Topological control of quantum states in non-Hermitian spin-orbit-coupled fermions

Zejian Ren,[1] Dong Liu,[1] Entong Zhao,[1] Chengdong He,[1] Ka Kwan Pak,[1] Jensen Li,[1,*] and Gyu-Boong Jo[1,†]

[1]*Department of Physics, The Hong Kong University of Science and Technology, Clear Water Bay, Kowloon, Hong Kong, China*

While spin-orbit coupling (SOC), an essential mechanism underlying quantum phenomena from the spin Hall effect to topological insulators [1, 2], has been widely studied in well-isolated Hermitian systems, much less is known when the dissipation plays a major role in spin-orbit-coupled quantum systems [3]. Here, we realize dissipative spin-orbit-coupled bands filled with ultracold fermions, and observe a parity-time ($\mathcal{PT}$) symmetry-breaking transition as a result of the competition between SOC and dissipation. Tunable dissipation, introduced by state-selective atom loss, enables the energy gap, opened by SOC, to be engineered and closed at the critical dissipation value, the so-called exceptional point (EP) [4]. The realized EP of the non-Hermitian band structure exhibits chiral response when the quantum state changes near the EP. This topological feature enables us to tune SOC and dissipation dynamically in the parameter space, and observe the state evolution is direction-dependent near the EP, revealing topologically robust spin transfer between different quantum states when the quantum state encircles the EP. This topological control of quantum states for non-Hermitian fermions provides new methods of quantum control, and also sets the stage for exploring non-Hermitian topological states with SOC.

Introduction An open quantum system that does not conserve energy is effectively described by a non-Hermitian Hamiltonian [3] and exhibits various counterintuitive phenomena that cannot exist when the system is Hermitian. One such example is the fundamental understanding of non-Hermitian topological matter that may require subtle classification in contrast to the Hermitian topological system, such as iconic topological insulators [1, 2]. Although extensive theoretical research [3, 5, 6] and recent experimental works [7–10] have been carried out on the non-Hermitian topological band, how the non-Hermitian topological state can be classified remains elusive. In particular, spin-orbit coupling (SOC), a key mechanism driving the non-trivial band topology, has not been investigated in non-Hermitian quantum systems. Recently, considerable efforts have been made in ultracold atom systems to explore synthetic SOCs [11–15] and associated topological bands [16–19], and therefore ultracold atoms offer the unprecedented possibility of studying the non-Hermitian SOC mechanism, a critical step toward realizing non-Hermitian topological phases [3].

In this work, we make an important step in this direction by realizing non-Hermitian spin-orbit-coupled quantum gases and oberving a parity-time ($\mathcal{PT}$) symmetry-breaking transition as a result of the competition between SOC and dissipation. We implement synthetic SOC for spin-1/2 ultracold fermions via the Raman transition [11] together with non-Hermiticity tunable in time. This controllability allows us to investigate how the energy spectrum of a spin-orbit-coupled system changes with dissipation and explore the $\mathcal{PT}$ symmetry-breaking transition across the exceptional point (EP) and its topological nature [4]. We measure the energy spectrum of the system via quasimomentum-resolved Rabi spectroscopy. Exploring the parameter regime from SOC-dominated to loss-dominated behavior, we identify an EP where the $\mathcal{PT}$ symmetry-breaking transition occurs in a fully quantum regime. Finally, we experimentally probe the chiral property of the EP by encircling it in a parameter space. We demonstrate that the state evolution is direction dependent near the EP, resulting in chiral quantum state transfer when encircling the EP due to the breakdown of adiabaticity. Our work sets the stage for the experimental study of many-body states in the complex energy bands across the $\mathcal{PT}$ symmetry-breaking transition, providing new methods of quantum control over the system. Recently, the feasibility of realizing many unprecedented phenomena in non-Hermitian atomic systems was noted, including enhanced fermionic superfluids [20], the generalized Floquet time crystal with dissipation [21] and higher-order topological phases [22], which cannot otherwise be observed in Hermitian systems.

This work complements the non-Hermitian phenomena observed in classical systems including topological energy transfer [23–25], enhanced sensing [26], $\mathcal{PT}$ symmetric lasing [27–29], and novel topological entities such as exceptional rings [30] and non-Hermitian topological edge states [31]. These developments have been made possible by the equivalence between the classical wave equation and the single-particle Schrodinger equation, but the role that non-Hermiticity plays in the genuine quantum regime ranging from few-body to many-body systems remains largely unexplored. Although recent works have explored non-Hermitian systems within a quantum framework [32] and have demonstrated the $\mathcal{PT}$ symmetry-breaking transition in non-Hermitian quantum systems, such as photons [33–35], superconducting qubits [36], single electronic spins [37] or free atoms [38, 39], the dynamic evolution of the quantum state near the EP has been limited to the single particle quantum system [40]. Here, we demonstrate the topological control of the quantum state with ultracold fermions showcasing the topological spin transfer between two quantum states.

General idea of the system Our experiment begins by loading ultracold fermions of ^{173}Yb atoms into the engineered energy band created in an optical dipole trap as described in previous works [17]. To create a non-Hermitian SOC Hamiltonian, we choose two hyperfine states of the ground state manifold of ^{173}Yb (labeled as the $|\uparrow\rangle$ and $|\downarrow\rangle$ states) that

*Electronic address: jensenli@ust.hk
†Electronic address: gbjo@ust.hk

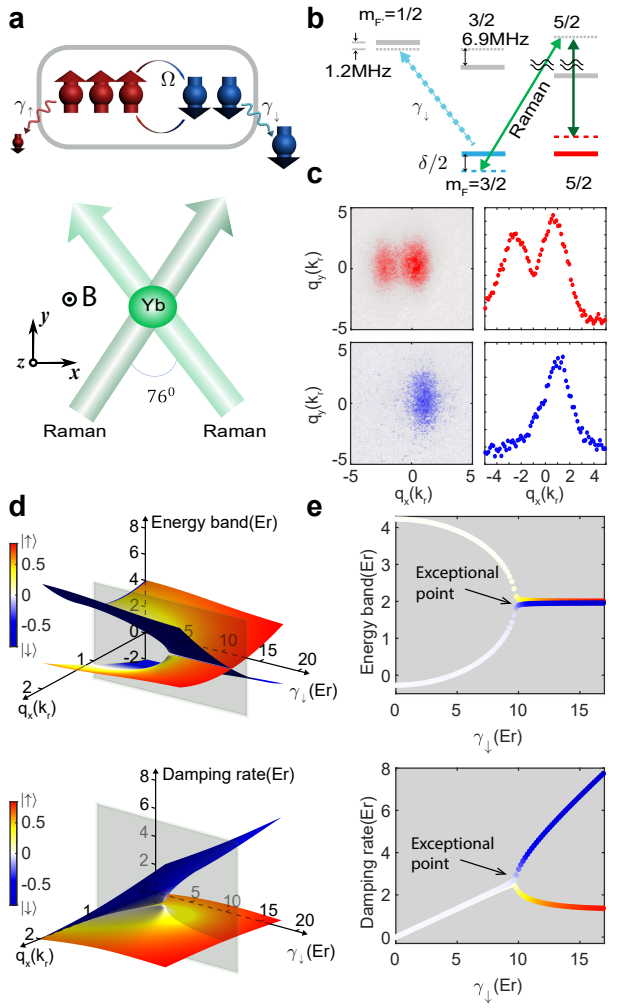

FIG. 1: **Non-Hermitian spin-orbit-coupled system of ultracold atoms** **a**, Our quantum system comprises ultracold fermions with two spin states, $|\uparrow\rangle$ (red) and $|\downarrow\rangle$ (blue), coupled by Raman beams (green arrow). Atom loss is controlled by additional light (not shown), resulting in spin-dependent loss $\gamma_{\uparrow,\downarrow}$. **b**, Schematic energy level diagram with relevant transitions. The atom loss beam is detuned by 1.2 MHz (6.9 MHz) from the $|m_F = 3/2\rangle \rightarrow |m_{F'} = 1/2\rangle$ transition ($|m_F = 5/2\rangle \rightarrow |m_{F'} = 3/2\rangle$ transition). **c**, Density distribution of $|\uparrow\rangle$ (red) and $|\downarrow\rangle$ (blue) atoms with SOC and its cross-sectional profile along the x direction after 6 ms time-of-flight expansion. **d**, Complex energy bands shown by the real and imaginary parts of $\lambda_\pm$ in the parameter space of quasimomentum (q_x) and dissipation ($\gamma_\downarrow$) for $\delta = 4E_r$ and $\Omega_R = 4.5E_r$. **e**, Energy band (Re($\lambda_\pm$)) and damping rate (Im($\lambda_\pm$)) showing the EP at $\gamma_\downarrow$=9.75E_r along $q_x = 1.0k_r$ (gray plane in (D)) when $2\Omega_R = (\gamma_\downarrow - \gamma_\uparrow)$.

are coupled by a pair of Raman transition beams intersecting at θ=76° and blue-detuned by ∼1 GHz. We implement controlled atom loss by adding σ^--polarized near-resonant 556 nm light whose scattering rate is spin dependent as depicted in Fig. 1a. The background heating arising from the Raman transition is negligible within the time scale of the experiment.

Synthetic SOC results in equal strengths of the Rashba and Dresselhaus SOC fields [11]. In a typical energy dispersion, the energy gap between two dressed bands is opened by Raman coupling Ω_R. Adding the spin-dependent atom loss $\gamma_{\uparrow,\downarrow}$, we realize a tunable non-Hermitian Hamiltonian,

$$\mathcal{H} = \begin{pmatrix} \frac{\hbar^2}{2m}(q_x - k_r)^2 + \delta/2 & \Omega_R/2 \\ \Omega_R/2 & \frac{\hbar^2}{2m}(q_x + k_r)^2 - \delta/2 \end{pmatrix} + \mathcal{H}_{loss}$$

where $\mathcal{H}_{loss} = -\frac{i}{2}(\gamma_\uparrow|\uparrow\rangle\langle\uparrow| + \gamma_\downarrow|\downarrow\rangle\langle\downarrow|)$, q_x is the quasimomentum of atoms along the $\hat{x}$-direction, m is the mass of the ytterbium atom, Ω_R is the Raman coupling strength, δ is the two-photon detuning and $\gamma_{\uparrow,\downarrow}$ is the spin-dependent atom loss. Here, we define natural units of momentum and energy as $\hbar k_r = \sin(\frac{\theta}{2})\frac{2\pi\hbar}{\lambda_{556}}$ and $E_r = \frac{\hbar^2 k_r^2}{2m}$=$h$×1.41 kHz, where λ_{556}=556 nm. Then, the real momentum k_x is related to the quasimomentum as $k_x = q_x \mp k_r$ for spin-up and spin-down, respectively. In our experiment, atom loss is induced by the single near-resonant beam (Fig. 1b), resulting in the fixed ratio of $\gamma_\downarrow/\gamma_\uparrow = 13$ (see more details in the Supplementary Materials). The change in δ due to the energy shift induced by the loss beam is less than h×0.1 kHz at $\gamma_\downarrow = 1E_r$.

The quantum dynamics of two dressed energy bands $\{|+\rangle, |-\rangle\}$, corresponding to the eigenvalues $\lambda_\pm$ of $\mathcal{H}$, are governed by the eigenvalue difference $\delta\lambda = (\lambda_+ - \lambda_-)$. In the parameter space comprising quasimomentum (q_x) and atom loss ($\gamma_\downarrow$), the $\mathcal{PT}$ symmetry-breaking transition occurs at the EP where both eigenvalues and eigenvectors coalesce as described in Fig. 1d and e. When the system is *Hermitian* with $\gamma_{\uparrow,\downarrow}$=0, the gap is opened at $q_x = (\frac{\delta}{4E_r})k_r$ due to the coupling between the two spin states [11]. With finite atom loss ($\gamma_{\uparrow,\downarrow} \neq 0$), however, the energy gap is reduced and eventually closed at the critical value (i.e., the EP), above which the eigenvalue difference becomes complex as Im($\delta\lambda$)≠0. Alternatively, the gain and loss can be understood as being balanced at the EP by gauging out $\frac{i}{2}(\gamma_\uparrow - \gamma_\downarrow)\sigma_I$ from $\mathcal{H}$ [4].

Momentum-sensitive Rabi spectroscopy To demonstrate the complex band structure of a non-Hermitian system, we investigate how the spin-orbit-coupled band is affected by dissipation by probing the energy spectrum via momentum-sensitive Rabi spectroscopy. We begin with a spin-polarized degenerate Fermi gas of 2×10^4 atoms in $|\uparrow\rangle$ without the Raman transition and loss (i.e., $\Omega_R = \gamma_{\uparrow,\downarrow} = 0$). Subsequently, $|\uparrow\rangle$ atoms are transferred to the $|\downarrow\rangle$ state when the Raman coupling is switched on (see Fig. 1c). When the two spin states $|\uparrow\rangle$ and $|\downarrow\rangle$ are coupled through the two-photon Raman transition, a nonuniform spin-orbit gap is opened between the two dressed states, resulting in Rabi oscillation. We detect this quasimomentum-dependent energy gap by monitoring the Rabi oscillation frequency at each quasimomentum in the experiment. In this measurement, brief pulses of the Raman coupling and loss beams are applied for a variable time duration followed by 6 ms ballistic expansion. The time-of-flight expansion maps momentum to real space, allowing direct momentum resolution of the energy band.

One of the features associated with dissipation is the closing of the energy gap at the EP [30]. Fig. 2a shows typical spin-orbit-coupled energy bands at different dissipation strengths for δ =$4E_r$ and their Rabi oscillations pulsing in the Raman

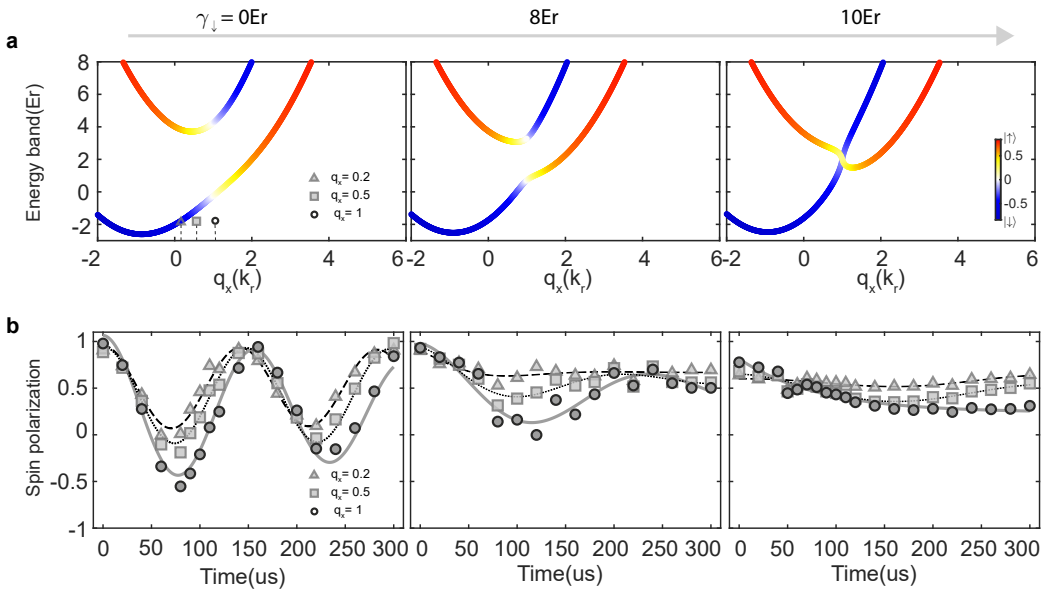

FIG. 2: **Momentum-resolved Rabi spectroscopy for observing band merging** **a**, Single-particle energy dispersion of dressed states with increasing dissipation. The energy gap at the resonant quasimomentum $q_x = 1.0k_r$ is closed above the EP at $\gamma_\downarrow$ =9.75E_r. **b**, Rabi oscillation for δ =+4E_r and Ω_R=4.5E_r. Atoms, prepared in $|\uparrow\rangle$, are suddenly projected into a superposition of eigenstates revealing a nonuniform energy gap.

field with dissipation for a variable duration (Fig. 2b), which reveals the nonuniform energy gap of the dressed bands. In the absence of atom loss ($\gamma_{\uparrow,\downarrow}$=0), the state undergoes Rabi oscillation subject to the energy of the gap at each quasimomentum. The Rabi coupling is resonant at $q_x = 1.0k_r$, revealing the smallest energy gap. The Rabi oscillation becomes slower with increasing dissipation. By fitting the spin oscillation with a damped sinusoidal function, we determine the energy gap and damping rate at each quasimomentum as described in Fig. 2b. The spin polarization is averaged taking into account the finite optical resolution over $\pm 0.15k_r$.

Observation of the $\mathcal{PT}$ symmetry-breaking transition To demonstrate the existence of the EP, we now investigate the associated $\mathcal{PT}$ symmetry-breaking transition, which occurs at $q_x = 1.0k_r$ where SOC is resonant. In our experiment, a Fermi sea occupying the band collectively undergoes Rabi oscillations in contrast to the non-Hermitian classical [4] or single-particle quantum [40] system, revealing a nonuniform band gap in time-dependent spin textures (see Fig. 3a). From this quasimomentum-dependent Rabi oscillation, we extract the energy gap, Re($\delta\lambda$), between two dressed bands for different dissipation strengths, as shown in Fig. 3b, in good agreement with the theoretical expectation. The dissipation gives rise to gap closing at the resonant coupling at q_x=1.0k_r, while the other quasimomenta still reveal a finite energy gap.

Fig. 3d and e show a quantitative measurement of the band gap (Re($\delta\lambda$)) and damping rate (Im($\delta\lambda$)) of the non-Hermitian system at q_x=1.0k_r, manifesting the $\mathcal{PT}$ symmetry-breaking transition. In the $\mathcal{PT}$ symmetric phase, the initial quantum state oscillates between two eigenstates of the non-Hermitian Hamiltonian (see Fig. 3c). Above the EP, however, the strong dissipation completely closes the energy gap with finite Im($\delta\lambda$) $\neq$0, giving rise to monotonic behavior, as shown in Fig. 3c. Both the band gap and damping rate show the $\mathcal{PT}$ symmetry-breaking transition near the EP at $\gamma_\downarrow$ =9.75E_r (see Fig. 3d,e). We can trace the energy gap at a nonresonant momentum, q_x=0.5k_r, as shown in the inset of Fig. 3d. In this case, the energy gap saturates to a finite energy gap. With large dissipation, the spin-orbit-coupled band structure becomes similar to free particle dispersion, which is consistent with the quantum Zeno effect.

Topological spin transfer by encircling the EP Having demonstrated the ability to engineer a spin-orbit-coupled energy band with dissipation, we now explore topological features near the EP by dynamically encircling it with fermions. Near the EP, the state evolution is direction dependent, resulting in intriguing chiral behavior when encircling the EP due to the breakdown of adiabaticity in non-Hermitian systems [4]. While this topological chirality has been observed in classical systems [23–25, 41–45], such as photonics and acoustics, it remains largely unexplored in quantum systems [40], especially in many-body quantum systems. In contrast to classical systems where encircling of the EP has often been performed along the spatially varying Hamiltonian, the quantum system with time-varying dissipation may allow for full Hamiltonian engineering capability.

Here, we demonstrate full time-varying control of a non-Hermitian Hamiltonian such that the EP is effectively encircled by ultracold fermions in different directions. This is enabled by the EP occurring at the quasimomentum $q_x = (\frac{\delta}{4E_r})k_r$ where SOC is resonant. This leads to control of the EP position along the q_x axis, effectively with respect to the Fermi sea in the dressed band, by tuning the two-photon detuning δ. In our experiment, we simultaneously tune the loss

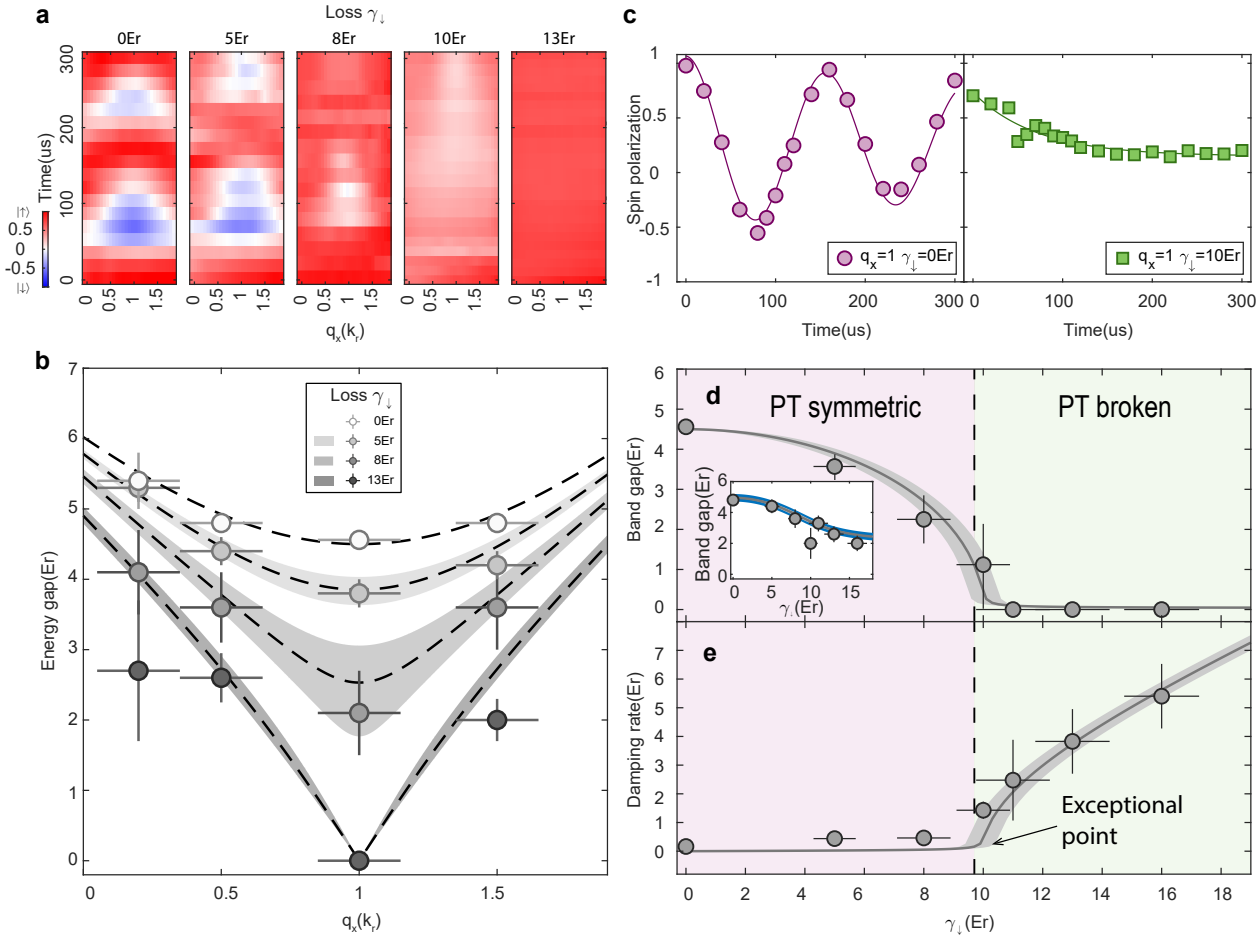

FIG. 3: $\mathcal{PT}$ **symmetry-breaking transition and band closing at the EP** **a**, Time-dependent spin texture obtained for different dissipation strengths. The quasimomentum-resolved spin polarization is monitored after switching on SOC fields with dissipation for a variable time. Each spin texture is averaged over 10 measurements. **b**, Energy band gap (circles) measured via Rabi spectroscopy, which is in good agreement with theory (dashed lines). The shaded region indicates the uncertainty in the theoretical band gap due to the uncertainty in the atom loss. **c**, Phase diagram of the $\mathcal{PT}$ symmetry-breaking transition from the unbroken phase with prominent Rabi oscillations (left) to the broken phase showing a monotonic spin polarization (right). Energy gap and damping rate measured from the Rabi oscillation shown with the real (**d**), and imaginary (**e**), eigenvalues of $\mathcal{H}$ (solid lines), respectively. The error bars in all panels represent standard fitting errors (vertical) and the experimental uncertainty related to the calibration (horizontal).

($\gamma_\downarrow$) and two-photon detuning (δ) and dynamically explore arbitrary paths in the complex band near the EP.

We begin with adiabatic loading of an ultracold Fermi gas into the lowest energy dressed band at $\delta = +3E_r$. In the initial quantum state, a Fermi sea is adiabatically formed at approximately $q_x \simeq -0.8k_r$ with the dominant spin component of $|\downarrow\rangle$ (blue color of energy band in Fig. 4), whereas the EP occurs at $q_x = (\frac{\delta}{4E_r})k_r$ =0.75k_r in the $q_x - \gamma_\downarrow$ parameter space. We now tune the two-photon detuning δ from +3E_r to -6E_r, which shifts the EP to q_x =-1.5k_r. Subsequently, the loss is increased from zero to different $\gamma_\downarrow^{max}$, followed by consecutive control of the two-photon detuning and loss. This results in counterclockwise encircling along a closed loop within T=10.1 ms in the $q_x - \gamma_\downarrow$ parameter space, as depicted in Fig. 4a (left), where T is the total encircling time (see the Supplementary Materials). By reversing the aforementioned process, we can encircle the EP in a clockwise manner.

Then, the spin polarization of the quantum state after the encircling process is determined via an optical Stern-Gerlach pulse followed by ballistic expansion. When the atom loss $\gamma_\downarrow$ is increased to $\gamma_\downarrow^{max}$=10 or 8 E_r, we observe that the initial quantum state of atoms with $|\downarrow\rangle$-dominant spin polarization is selectively switched to spin up depending on the encircling direction in Fig. 4b. This observation reveals that the evolution of the quantum state switches the state to a different eigenstate near the EP [25] depending on the encircling direction within the complex energy surface. The topological spin transfer disappears for $\gamma_\downarrow^{max}$=2 E_r if the EP is located far from the loop, as depicted in Fig. 4c showing no chiral behavior.

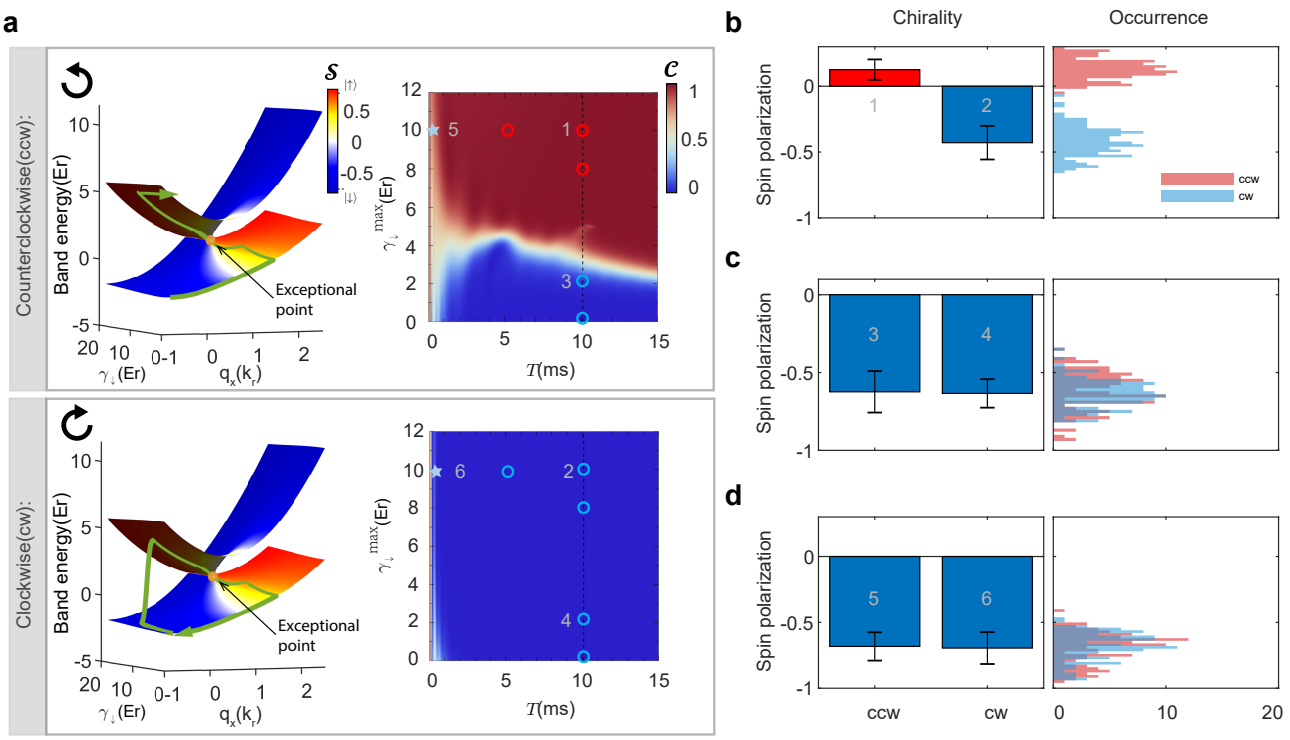

FIG. 4: **Topological chiral spin transfer by dynamically encircling an EP** **a**, A Fermi gas is first adiabatically prepared in the initial $|\downarrow\rangle$-dominated state (spin polarization indicated by blue) in the parameter space with $\gamma_\downarrow = 0E_r$ and $\delta = 3E_r$ (left panel). We effectively encircle the EP with fermions by tuning the loss and two-photon detuning (green arrow). The spin polarization before dynamic encircling is approximately -0.7 in the initial state. The right panel of (a) shows expected state conversion efficiency $\mathcal{C}$ from $|\downarrow\rangle$ to $|\uparrow\rangle$ against loop duration time T and the maximum atom loss $\gamma_\downarrow^{max}$ for the counterclockwise (top) and clockwise (bottom) encircling in the parameter space. The dominant spin polarization of the quantum state measured after the encircling is indicated by the color of the circles and stars. The final spin polarization after encircling is experimentally measured for different T and $\gamma_\downarrow^{max}$ as indicated by the colour of the circle or star, after following the trajectory along clockwise (CW) and counterclockwise (CCW) closed loops. **b-c**, show the chiral behavior of final spin polarization for the experimental configurations indicated as circles with the same indices in (a). For other values of T, we keep the same fraction of time for each edge of the trajectory as in the experiment. **d**, No chirality is observed when dynamic encircling is instantaneous within 0.04 ms corresponding to solid star in the right panel of (a). For all cases of (b-d), corresponding histograms for the 100 consecutive measurement series with a binning width of 0.02 for spin polarization are shown. The error bar represents the standard deviation of the measurements.

To better understand the quantum dynamics during the nonadiabatic evolution, we perform additional numerical calculations in a larger domain of accessible parameters in $\gamma_\downarrow^{max}$ and duration of the whole loop (see the detailed model in the Supplementary Materials). The state conversion efficiencies $\mathcal{C}$ for encircling in the two directions are plotted as two color maps in Fig. 4a. The experimental results in Fig. 4b and c (labeled 1 to 4) are indicated by circles at T=10.1 ms, in good agreement with $\mathcal{C} \gg 0$ for the case 1 and $\mathcal{C}$=0 for the other cases. In fact, a smaller encircling speed (i.e., a larger T) increases the chance of nonadiabatic transitions as long as the trajectory runs near the EP and further lowers the transition threshold of $\gamma_\downarrow^{max}$ [25]. The chiral behavior is also observed for T=5 ms. On the other hand, we find the inability of the system to adapt to the rapidly varying parameters when T ~0.04 ms is small as Fig. 4d (labeled 5 and 6). A more detailed classification of the behavior of $\mathcal{C}$ in different phases is given in the Supplementary Materials.

Conclusion In this work, we have experimentally demonstrated how non-Hermiticity essentially affects the dispersion relation of spin-orbit-coupled fermions. The $\mathcal{PT}$ symmetry-breaking transition has been identified through spectroscopy of the complex energy band and the chiral spin transfer around the EP. The topological nature near the EP indicates that non-Hermiticity can fundamentally modify the physical properties of the spin-orbit-coupled quantum system. Investigating how the interplay between two mechanisms - SOC and non-Hermiticity - may bring about new quantum phenomena, such as non-Hermitian topological phases in Bloch bands [6], will be interesting. In contrast to classical systems where only single (bosonic) particle dynamics are considered, our system sets the stage for investigating many-body interacting fermions with dissipation [46, 47]. Furthermore, the possibility of exploring nonequilibrium dynamics, quantum thermodynamics [48] and information criticality [49] across the $\mathcal{PT}$ symmetry-breaking transition by engineering the non-Hermitian Hamiltonian in a dynamic manner is conceivable. Our experimental method can be broadly applied to other systems, such as spin-orbit-coupled bosons [11–13], and can provide a new approach to the topological quantum control.

Acknowledgments

Funding G.-B.J. acknowledges support from the RGC and the Croucher Foundation through 16305317, 16304918, 16306119, 16302420, C 6005-17G and N-HKUST601/17. J.L. acknowledges support from the RGC through 16304520 and C6013-18G.

Competing interests The authors declare no competing interests

Data and materials availability The data that support the finding of this work are available from the corresponding authors upon reasonable request.

[1] M. Hasan and C. Kane, *Reviews of Modern Physics* **82**, 3045 (2010).
[2] X.-L. Qi and S.-C. Zhang, *Reviews of Modern Physics* **83**, 1057 (2011).
[3] Y. Ashida, Z. Gong and M. Ueda, *arXiv.org* **2006**, arXiv:2006.01837 (2020).
[4] M.-A. Miri and A. Alu, *Science* **363**, eaar7709 (2019).
[5] Z. Gong, Y. Ashida, K. Kawabata, K. Takasan, S. Higashikawa and M. Ueda, *Physical Review X* **8**, (2018).
[6] S. Yao, F. Song and Z. Wang, *Physical review letters* **121**, 136802 (2018).
[7] T. Helbig, T. Hofmann, S. Imhof, M. Abdelghany, T. Kiessling, L. W. Molenkamp, C. H. Lee, A. Szameit, M. Greiter and R. Thomale, *Nature Physics* **16**, 747 (2020).
[8] L. Xiao, T. Deng, K. Wang, G. Zhu, Z. Wang, W. Yi and P. Xue, *Nature Physics* **16**, 761 (2020).
[9] A. Ghatak, M. Brandenbourger, J. v. Wezel and C. Coulais, *Proceedings of the National Academy of Sciences* **117**, 29561 (2020).
[10] S. Weidemann, M. Kremer, T. Helbig, T. Hofmann, A. Stegmaier, M. Greiter, R. Thomale and A. Szameit, *Science* **368**, 311 (2020).
[11] Y.-J. Lin, K. Jimenez-Garcia and I. B. Spielman, *Nature* **471**, 83 (2011).
[12] J.-Y. Zhang, S.-C. Ji, Z. Chen, L. Zhang, Z.-D. Du, B. Yan, G.-S. Pan, B. Zhao, Y.-J. Deng, H. Zhai et al., *Physical Review Letters* **109**, 115301 (2012).
[13] C. Qu, C. Hamner, M. Gong, C. Zhang and P. Engels, *Physical Review A* **88**, 021604 (2013).
[14] P. Wang, Z.-Q. Yu, Z. Fu, J. Miao, L. Huang, S. Chai, H. Zhai and J. Zhang, *Physical Review Letters* **109**, 095301 (2012).
[15] L. W. Cheuk, A. T. Sommer, Z. Hadzibabic, T. Yefsah, W. S. Bakr and M. W. Zwierlein, *Physical Review Letters* **109**, 095302 (2012).
[16] Z. Wu, L. Zhang, W. Sun, X.-T. Xu, B.-Z. Wang, S.-C. Ji, Y. Deng, S. Chen, X.-J. Liu and J.-W. Pan, *Science* **354**, 83 (2016).
[17] B. Song, L. Zhang, C. He, T. F. J. Poon, E. Hajiyev, S. Zhang, X.-J. Liu and G.-B. Jo, *Science advances* **4**, eaao4748 (2018).
[18] B. Song, C. He, S. Niu, L. Zhang, Z. Ren, X.-J. Liu and G.-B. Jo, *Nature Physics* **15**, 911 (2019).
[19] Z.-Y. Wang, X.-C. Cheng, B.-Z. Wang, J.-Y. Zhang, Y.-H. Lu, C.-R. Yi, S. Niu, Y. Deng, X.-J. Liu, S. Chen et al., *Science* **372**, 271 (2021).
[20] K. Yamamoto, M. Nakagawa, K. Adachi, K. Takasan, M. Ueda and N. Kawakami, *Physical review letters* **123**, (2019).
[21] A. Lazarides, S. Roy, F. Piazza and R. Moessner, *Physical Review Research* **2**, 022002 (2020).
[22] X.-W. Luo and C. Zhang, *Physical review letters* **123**, (2019).
[23] H. Xu, D. Mason, L. Jiang and J. G. E. Harris, *Nature* **537**, 80 (2016).
[24] J. Doppler, A. A. Mailybaev, J. Bohm, U. Kuhl, A. Girschik, F. Libisch, T. J. Milburn, P. Rabl, N. Moiseyev and S. Rotter, *Nature* **537**, 76 (2016).
[25] A. U. Hassan, G. L. Galmiche, G. Harari, P. LiKamWa, M. Khajavikhan, M. Segev and D. N. Christodoulides, *Physical Review A* **96**, 052129 (2017).
[26] J. Wiersig, *Physical Review Letters* **112**, 203901 (2014).
[27] M. Liertzer, L. Ge, A. Cerjan, A. D. Stone, H. E. Türeci and S. Rotter, *Physical Review Letters* **108**, 173901 (2012).
[28] H. Hodaei, M.-A. Miri, M. Heinrich, D. N. Christodoulides and M. Khajavikhan, *Science* **346**, 975 (2014).
[29] L. Feng, Z. J. Wong, R.-M. Ma, Y. Wang and X. Zhang, *Science* **346**, 972 (2014).
[30] B. Zhen, C. W. Hsu, Y. Igarashi, L. Lu, I. Kaminer, A. Pick, S. L. Chua, J. D. Joannopoulos and M. Soljacic, *Nature* **525**, 354 (2015).
[31] H. Zhao, X. Qiao, T. Wu, B. Midya, S. Longhi and L. Feng, *Science* **365**, 1163 (2019).
[32] F. Minganti, A. Miranowicz, R. W. Chhajlany and F. Nori, *Physical Review A* **100**, 062131 (2019).
[33] L. Xiao, X. Zhan, Z. H. Bian, K. K. Wang, X. Zhang, X. P. Wang, J. Li, K. Mochizuki, D. Kim, N. Kawakami et al., *Nature Physics* **13**, 1117 (2017).
[34] L. Xiao, K. Wang, X. Zhan, Z. Bian, K. Kawabata, M. Ueda, W. Yi and P. Xue, *Physical review letters* **123**, (2019).
[35] F. E. Ozturk, T. Lappe, G. Hellmann, J. Schmitt, J. Klaers, F. Vewinger, J. Kroha and M. Weitz, *Science* **372**, 88 (2021).
[36] M. Naghiloo, M. Abbasi, Y. N. Joglekar and K. W. Murch, *Nature Physics* **15**, 1232 (2019).
[37] Y. Wu, W. Liu, J. Geng, X. Song, X. Ye, C.-K. Duan, X. Rong and J. Du, *Science* **364**, 878 (2019).
[38] J. Li, A. K. Harter, J. Liu, L. d. Melo, Y. N. Joglekar and L. Luo, *Nature Communications* **10**, 855 (2019).
[39] Y. Takasu, T. Yagami, Y. Ashida, R. Hamazaki, Y. Kuno and Y. Takahashi, *Progress of Theoretical and Experimental Physics* **2020**, ptaa094 (2020).
[40] W. Liu, Y. Wu, C.-K. Duan, X. Rong and J. Du, *arXiv* **2020**, (2020).
[41] A. A. Mailybaev, O. N. Kirillov and A. P. Seyranian, *Physical Review A (Atomic, Molecular, and Optical Physics)* **72**, 014104 (2005).
[42] R. Uzdin, A. Mailybaev and N. Moiseyev, *Journal of Physics A: Mathematical and Theoretical* **44**, 435302 (2011).
[43] J. H. Wu, M. Artoni and G. C. L. Rocca, *Physical review letters* **113**, 123004 (2014).
[44] T. Gao, E. Estrecho, K. Y. Bliokh, T. C. H. Liew, M. D. Fraser, S. Brodbeck, M. Kamp, C. Schneider, S. Hofling, Y. Yamamoto et al., *Nature* **526**, 554 (2015).
[45] J. W. Yoon, Y. Choi, C. Hahn, G. Kim, S. H. Song, K.-Y. Yang, J. Y. Lee, Y. Kim, C. S. Lee, J. K. Shin et al., *Nature* **562**, 86 (2018).
[46] L. Zhou and X. Cui, *iScience* **14**, 257 (2019).

[47] L. Zhou, W. Yi and X. Cui, *Physical Review A* **102**, 043310 (2020).
[48] S. Deffner and A. Saxena, *Physical Review Letters* **114**, 150601 (2015).
[49] K. Kawabata, Y. Ashida and M. Ueda, *Physical Review Letters* **119**, 190401 (2017).

Supplementary Material

S-1. Experimental details

A. Preparation of the sample

We slow down ^{173}Yb atoms through the two-stage process [1] and pre-cool them in the intercombination magneto-optical trap [2]. We then begin with the experiment for a two-component degenerate ^{173}Yb Fermi gas of 2×10^4 atoms and prepared at $T/T_F \lesssim 0.3(1)$ following forced evaporative cooling in an optical dipole trap formed by 1064 nm and 532 nm laser beams with a trap frequency of $\bar{\omega} = (\omega_x\omega_y\omega_z)^{1/3}$ =112×2π Hz. Here $|\uparrow,\downarrow\rangle = |m_F = 5/2, m_F = 3/2\rangle$ represent hyperfine states of the ground manifold. A quantized axis is fixed by the bias magnetic field of 13.6 G along the z direction. Typically, before the spin-orbit coupling is switched on by a pair of two-photon Raman beams, two hyperfine levels ($|\uparrow\rangle$,$|\downarrow\rangle$) are isolated from other states (i.e. $m_F = 1/2, -1/2, -3/2$ and $-5/2$) using the spin-dependent light shift induced by the σ^- polarized beam (referred to a lift beam), blue-detuned by $\sim$1 GHz, which lifts the degeneracy of the ground manifold.

B. Control of atom loss

To control the dissipation of the system, we use a dedicated plane-wave laser beam (referred to loss beam) at a small detuning around the narrow intercombination transition $^1\mathrm{S}_0(F = \frac{5}{2}) \leftrightarrow {}^3\mathrm{P}_1(F' = \frac{7}{2})$ with the natural linewidth of 182 kHz. The loss beam is σ^- polarized, and is detuned by 1.2 MHz and 6.9 MHz with respect to $|m_F = 3/2\rangle \rightarrow |m_{F'} = 1/2\rangle$ and $|m_F = 5/2\rangle \rightarrow |m_{F'} = 3/2\rangle$ transitions, respectively, which results in spin-sensitive photon scattering. The detuning of the loss beam is chosen such that the light is essentially resonant for atoms in the $|m_F = 3/2\rangle = |\downarrow\rangle$ state with the fixed ratio of $\gamma_\downarrow/\gamma_\uparrow$=13. Although the absorption and reemission of a photon can leave an atom back in its original state, for example, with the probability of $\sim$14% for atoms in $|\downarrow\rangle$ (see the relative optical transition strength between hyperfine states in Fig. S1a), we define the effective photon scattering rate as the genuine one-body dissipation ignoring the heating effect which is not significant in our current experimental regime. We expect the heating associated with the photon scattering can be further suppressed by pumping excited atoms in the $^3\mathrm{P}_1$ manifold to $^3\mathrm{S}_1$ with 680 nm light [3]. We calibrate the photon scattering rate γ_σ by fitting a function $e^{-\gamma_\sigma t}$ to the atom number of the state $|\sigma =\uparrow,\downarrow\rangle$ after the loss beam is suddenly switched on (see Fig. S1). We achieve tunable loss rate by controlling the power of the loss beam.

C. Encircle the exceptional points

We dynamically control the non-Hermitian Hamiltonian and effectively encircle the exceptional point by ultracold fermions in the parameter space. Fig. S2 shows the experimental sequence of adjusting the two-photon detuning δ and the loss $\gamma_\downarrow$ after the spin-orbit coupling is adiabatically switched on at $\delta = 3E_r$. We achieve clockwise encircling (CW) by increasing the loss to $\gamma_\downarrow^{max}$=10 E_r within 100 μs followed by the change of two-photon detuning from $\delta = 3E_r$ to $\delta = -6E_r$ over 1 ms. Subsequently, we decrease the loss to $0E_r$ within 4 ms and adjust the two-photon detuning to the original value within 5 ms, which results in the clockwise loop in the parameter space. The counterclockwise (CW) encircling loop can be realized by reversing the above-mentioned process. In our experiment, we minimize the time duration of the $\delta >0$ region where $|\downarrow\rangle$ atoms are dominant (e.g., from the point (1) to (2) in Fig. S2) and consequently minimize the atom number loss which is essentially for fthe $|\downarrow\rangle$ state.

S-2. Evolution of the quantum state along the rectangular trajectory

In a spin-up ($|\uparrow\rangle$) and spin-down ($|\downarrow\rangle$) basis, two-photon detuning and spin-dependent atomic loss in our non-Hermitian Hamiltonian in the main text is time-varying. In this numerical analysis, we take dimensionless quantities: $\tau = t/t_R, \tilde{q_x} = q_x/k_r, \widetilde{\Omega}_R = \Omega_R/E_r, \tilde{\delta} = \delta/E_r, \tilde{\gamma}_\uparrow = \gamma_\uparrow/E_r$ and $\tilde{\gamma}_\downarrow = \gamma_\downarrow/E_r$, where $t_R = \frac{2m}{\hbar k_r^2} \approx 0.113ms$ and E_r is the recoil energy. The Hamiltonian can then be rewritten as

$$\mathcal{H}(\tau) = \begin{pmatrix} (\tilde{q}_x - 1)^2 + \frac{\tilde{\delta}(\tau)}{2} - i\frac{\tilde{\gamma}_\uparrow(\tau)}{2} & \widetilde{\Omega}_R/2 \\ \widetilde{\Omega}_R/2 & (\tilde{q}_x + 1)^2 - \frac{\tilde{\delta}(\tau)}{2} - i\frac{\tilde{\gamma}_\downarrow(\tau)}{2} \end{pmatrix}, \tag{S1}$$

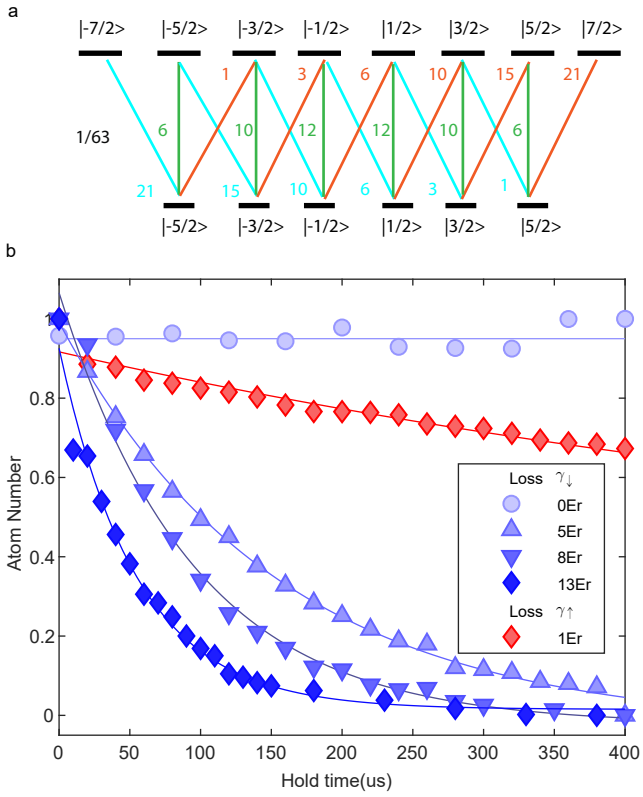

FIG. S1: **Calibration of of spin-sensitive atomic loss** (a) Relative optical transition strength between hyperfine states. (b) Atom number loss is calibrated for the spin-down state (blue shapes) at variable intensity of the loss beam. For comparison, the atom number of the spin-up state (red diamond) is shown when the atom loss is set at $\gamma_\downarrow^{max}$=13E_r (blue diamond).

with the time-dependent state $\psi(\tau) = \psi_\uparrow(\tau)|\uparrow\rangle + \psi_\downarrow(\tau)|\downarrow\rangle$ at any time τ. From this point onwards, we will drop the " $\sim$ " for simplicity in notations and we always express in terms of the dimensionless quantities. The location of the Fermi sea is kept approximately at a constant $q_x \cong -0.81$, as prepared initially in experiments. Raman coupling strength is kept constant at $\Omega_R = 4.5E_r$ while the two photon detuning $\delta(\tau)$ and atom loss $\gamma_\uparrow(\tau) = \gamma_\downarrow(\tau)/13$ are time-dependent. Considering the band transition associated with the time-dependent state, the phase information of the final state is irrelevant and therefore we take away the trace of the Hamiltonian:

$$i\frac{\partial}{\partial\tau}\psi(\tau) = \mathcal{H}(\tau)\psi(\tau), \quad \mathcal{H}(\tau) = \begin{pmatrix} -2\kappa + i\gamma & \Omega_R/2 \\ \Omega_R/2 & 2\kappa - i\gamma \end{pmatrix} \tag{S2}$$

with $\kappa = q_x - \delta/4, \gamma = (\gamma_\downarrow - \gamma_\uparrow)/4$. The two bands of $\mathcal{H}$ are denoted to have eigenvalues $\lambda_{1,2} = \mp\sqrt{(2\kappa - i\gamma)^2 + \Omega_R^2/4}$, eigenstates $|\psi_1\rangle$ for the lower state (band index 1) and $|\psi_2\rangle$ for the upper state (band index 2). From the form of eigenvalue, the EP emerges when $\kappa = 0$ and $\gamma = \Omega_R/2$, (corresponding to $\gamma_\downarrow = 9.75, \gamma_\uparrow = 0.75$ in our experiment).

The state is numerically evolved for any given trajectory of $(\kappa, \gamma_\downarrow)$ in a two dimensional parameter space as $\psi(\tau) = c_1(\tau)|\psi_1\rangle + c_2(\tau)|\psi_2\rangle$. Then, we can obtain the expected energy value at any particular moment by

$$\lambda(\tau) = \frac{\lambda_1 |c_1(\tau)|^2 + \lambda_2 |c_2(\tau)|^2}{|c_1(\tau)|^2 + |c_2(\tau)|^2} \tag{S3}$$

which allows us the plot the trajectory by using its real part as the green arrows in Fig. 4 in the main text. Similarly, the expected band index (-1 for the lower band $|\psi_1\rangle$ and +1 for the upper band $|\psi_2\rangle$) can be defined as

$$\mathcal{B}(\tau) = \frac{|c_2(\tau)|^2 - |c_1(\tau)|^2}{|c_1(\tau)|^2 + |c_2(\tau)|^2} \tag{S4}$$

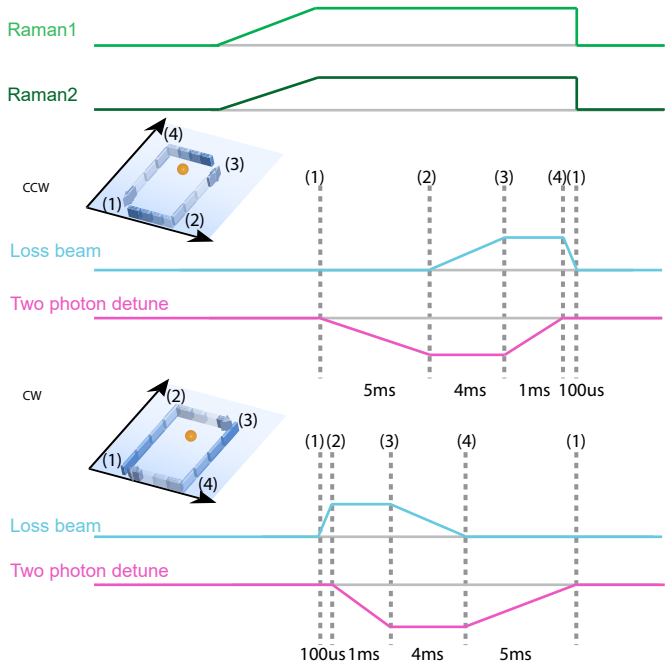

FIG. S2: **Experimental procedure for encircling the exceptional point** Before encircling the exceptional points, the atoms are adiabatically loaded on the (1) state by linealy increasing the two Raman beam with $\delta = 3Er$ and $\gamma_\downarrow = 0Er$. By changing the the δ and $\gamma_\downarrow$ as the picture, we achieve the atoms encircle the EP countclockwise and clockwise. The time scale is shown as the picture.

while the conversion efficiency $(\mathcal{C})$ from an initial state of index i_0 to the opposite state of index $3 - i_0$ is related to the band index by

$$\mathcal{C}\left(i_0\right) = \frac{\left|c_{3-i_0}(T)\right|^2}{\left|c_1(T)\right|^2 + \left|c_2(T)\right|^2} = \frac{1 + (3 - 2i_0)\,\mathcal{B}}{2} \tag{S5}$$

after the completion of one closed loop of duration T. In the main text, we also plot the spin-imbalance (or spin-polarization) as

$$\mathcal{S}(\tau) = \frac{\left|\psi_\uparrow(\tau)\right|^2 - \left|\psi_\downarrow(\tau)\right|^2}{\left|\psi_\uparrow(\tau)\right|^2 + \left|\psi_\downarrow(\tau)\right|^2} \tag{S6}$$

which is defined similarly as the $\mathcal{B}$ but in terms of the original spin-up and spin-down basis rather than the eigenstates.

It is well known that chiral behavior can be associated to encircling an exceptional point, due to the structure of Riemann surface and non-adiabatic transition. Chiral behavior can also happen for a loop without encircling an exceptional point [4], and it depends much on the shape of the loop and also the speed of encircling. Here, we numerically examine the encircling trajectory used in the experiment of Fig. 4(b) and (c) of the main text. In Fig. S3, the numbers in red color denote the fractional duration of each edge in terms of the total duration T. The initial state is set at $\kappa = -1.56$ $(i.e., q_x \equiv -0.81, \delta = 3)$, $\gamma_\downarrow = 0$. The exceptional point is located at $(\kappa, \gamma_\downarrow) = (0, 9.75)$. When $\gamma_\downarrow^{max}$, the height of the loop, has a value of 10 (Fig. 4(b) in main text), the exceptional point is encircled. We also consider various $\gamma_\downarrow^{max}$ up to the value of 2 (see Fig. 4(c) in main text).

S-3. State conversion efficiency for variable T and $\gamma_\downarrow^{max}$

In Fig. S4, we plot the simulated state conversion efficiency $\mathcal{C}$ against the encircling speed defined as $v = 2\pi/T$ when we start from the lower/upper state in panels (a)/(b) for encircling in the clockwise direction and (c)/(d) for encircling in the counterclockwise direction, respectively. The experimental results in Fig. 4(b) and (c) in the main text corresponds to a fixed total duration $T = 89.4$ $(\log v = -2.66)$ in the various curves at different $\gamma_\downarrow^{max}$. When v is changed, we keep the ratio of time spent on each line as the red numbers labeled in Fig. S3. A value of conversion efficiency $\mathcal{C}$ approaching 1 (0) means the

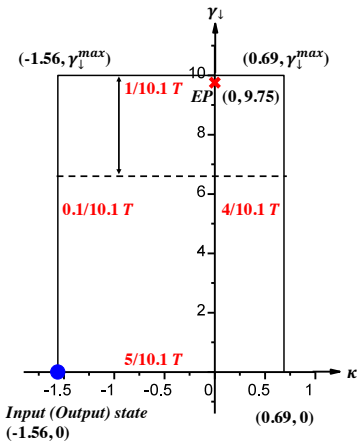

FIG. S3: **The trajectory in encircling exceptional point in the $\kappa - \gamma_\downarrow$ parameter space**. The location of input state and output state is (-1.56, 0), denoted by the blue point. The exceptional point lies in (0, 9.75), denoted by the red cross. The red number besides each line is the ratio of time spent on it.

state changes from one band to the other (the same) band after a complete loop of encircling. The results allow us to classify the behavior of $\mathcal{C}$ into different phases. When the encircling speed is large enough (in the region colored by gray), the state cannot react to the time-varying parameters and no state conversion ($\mathcal{C} \cong 0$) is observed in all the cases of different $\gamma_\downarrow^{max}$ in this "zero-reaction" phase (also shown in Fig. 4(d) in the main text). On the other hand, by lowering the encircling speed, the behavior of $\mathcal{C}$ passes through an oscillatory phase (cyan color), and goes into the chiral phase (green color). In the chiral phase, the final state is always ψ_1 in the clockwise direction and ψ_2 in the counter clockwise direction, independent of the initial state. It is revealed in Fig. S4(a) to (d) by $(\mathcal{C}_{\rm CW}(1), \mathcal{C}_{\rm CW}(2), \mathcal{C}_{\rm CCW}(1), \mathcal{C}_{\rm CCW}(2))$ approaching (0,1,1,0) in the green region. We note that the right edge of the green region of the chiral phase in Fig. S4 is set according to the case $\gamma_\downarrow^{max} = 12$ for guiding eyes. In fact, the onset of the chiral phase (how small the encircling speed has to be) depends on how close the upper edge of the trajectory towards the exceptional point. It is interesting to note that chiral behavior still occurs close to the exceptional point without encircling it [4].

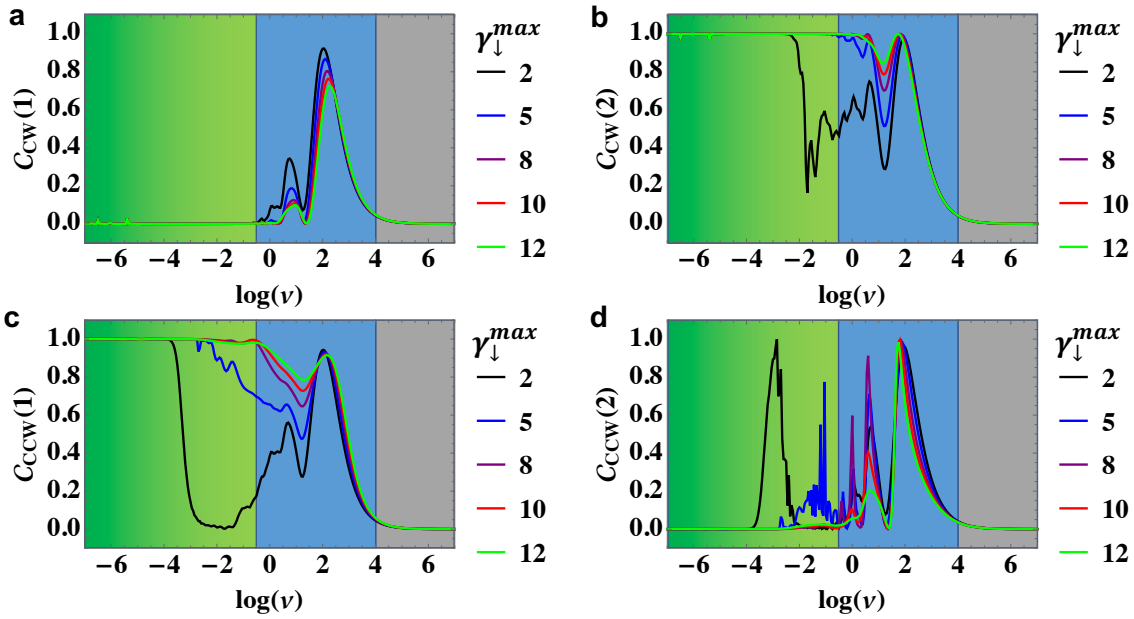

FIG. S4: **State conversion efficiency**. State conversion efficiency $(\mathcal{C})$ against encircling speed v in the clockwise direction (a) with initial state ψ_1 and (b) with initial state ψ_2. Similar results in the counterclockwise direction are obtained in (c) and (d). Different curves in the same panel correspond to rectangular loops with different $\gamma_{\downarrow}^{max}$. The colored regions indicate the chiral (green), oscillatory (cyan) and the zero-reaction (gray) behaviour of conversion efficiency for variable encircling speed v.

[1] B. Seo, P. Chen, Z. Chen, W. Yuan, M. Huang, S. Du, and G.-B. Jo, Physical Review A 102, 013319 (2020).

[2] B. Song, C. He, S. Zhang, E. Hajiyev, W. Huang, X.-J. Liu, and G.-B. Jo, Physical Review A 94, 061604 (2016).

[3] Y. Takasu, T. Yagami, Y. Ashida, R. Hamazaki, Y. Kuno, and Y. Takahashi, Prog Theor Exp Phys 2020, ptaa094 (2020).

[4] A. U. Hassan, B. Zhen, M. Soljacic, M. Khajavikhan, and D. N. Christodoulides, Phys. Rev. Lett. 118, 093002 (2017).